Chemical Engineering Journal 535 (2026) 175068

Contents lists available at ScienceDirect

Chemical Engineering Journal

journal homepage: www.elsevier.com/locate/cej

Dynamic and electrified ammonia synthesis enabled by magnetic heating of barium-promoted ruthenium catalyst

A. Sedminek [a,b,**], D. Makovec [a], M. Huš [c,d], A. Prašnikar [d], S. Yakushkin [d], B. Likozar [d,*], J. Teržan [d,*], S. Gyergyek [a,*]

[a] Jožef Stefan Institute, Jamova 39, 1000, Ljubljana, Slovenia
[b] Faculty of Chemistry and Chemical Technology, Smetanova 17, 2000, Maribor, Slovenia
[c] Association for Technical Culture of Slovenia (ZOTKS), Založka 65, 1000, Ljubljana, Slovenia
[d] National Institute of Chemistry, Hajdrihova 19, 1000 Ljubljana, Slovenia

ARTICLE INFO

Keywords:
Magnetic heating
Ammonia synthesis
Barium promoted catalyst
Electrification

ABSTRACT

Ammonia synthesis is a cornerstone of the chemical industry, but conventional methods rely on energy-intensive processes coupled to fossil fuels. Electrified, dynamically responsive ammonia synthesis that can rapidly adapt to fluctuating operating conditions, especially power input, is highly sought after to align with intermittent renewable energy sources such as solar or wind. Here, we demonstrate that a well-designed magnetic nanocatalyst – specifically, a Ba-promoted, Ru-decorated $Co_{0.67}Ni_{0.33}$-Al_2O_3 nanocomposite – provides localized heating at active sites. This enables rapid start-up (less than 10 min to achieve maximal ammonia productivity), a high synthesis rate exceeding 1500 mmol NH_3 g_{Ru}^{-1} h^{-1} at 350 °C and 5.5 MPa, and stable operation for at least 120 h. Kinetic analysis combined with calorimetric measurements reveals that magnetic heating induces pronounced local overheating, with effective temperatures at the catalytically active sites exceeding the thermocouple-measured bed temperature by more than 100 °C. This significant local overheating provides a mechanistic explanation for the observed high reaction rates and rapid dynamic response. Density functional theory and microkinetic modelling show that Ba promotion lowers the nitrogen dissociation barrier at Ru–BaO interfaces, enhancing activity. Our results highlight the synergistic role of magnetic heating and the Ru–BaO interface in accelerating ammonia synthesis under mild conditions and establish a foundation for dynamic, sustainable catalysis powered by renewable electricity.

1. Introduction

Over the past decade, the impact of climate change has driven the transition from fossil fuels to renewable energy (RE) sources. Effective storage and transport are critical for RE adoption. Hydrogen is a promising energy vector to address the intermittency of solar and wind energy, but it requires cryogenic storage (−253 °C, 0.1 MPa), has low volumetric energy density (8.49 kJ L^{-1}), and lacks well-developed storage and distribution infrastructure [1]. To overcome the required extreme conditions, hydrogen storage in a molecule such as ammonia is a promising alternative. Ammonia, as the hydrogen carrier, contains 17.8 wt% of hydrogen. It can be stored and transported as a liquid at −33 °C and 0.1 MPa, utilize existing infrastructure, and possess a higher volumetric energy density (12.92 kJ L^{-1}) than liquefied hydrogen [2,3].

As industrial ammonia production using the Haber-Bosch process is very energy-intensive, alternatives based on renewable energies - such as electrochemical, photochemical, and plasma-based processes - have been developed to improve the carbon footprint [4,5]. While these approaches still face major challenges in terms of catalyst design, energy efficiency, and cost-effectiveness, the development of new materials and technologies promises their further development into environmentally friendly and viable alternatives [4,6–8]. Furthermore, these innovations open up opportunities for decentralised ammonia production.

One particularly innovative approach is magnetically heated catalysis, a non-contact heating technique in which magnetic nanoparticles are integrated into catalysts to generate localized heat via hysteresis losses when exposed to alternating magnetic field (AMF). Compared to external thermal heating, magnetic heating enables localized and rapid

* Corresponding author.
** Correspondence to: A. Sedminek, Jožef Stefan Institute, Jamova 39, 1000, Ljubljana, Slovenia.
E-mail addresses: anja.sedminek@ijs.si (A. Sedminek), blaz.likozar@ki.si (B. Likozar), janvit.terzan@ki.si (J. Teržan), saso.gyergyek@ijs.si (S. Gyergyek).

https://doi.org/10.1016/j.cej.2026.175068
Received 25 November 2025; Received in revised form 16 January 2026; Accepted 8 March 2026
Available online 11 March 2026

energy delivery directly within the catalytic bed, thereby overcoming heat-transfer limitations and thermal inertia in the reactor. As a result, higher effective local temperatures, faster thermal response, and enhanced reaction rates can be achieved. Additionally, dynamic temperature control facilitates flexible operation, improved safety, simplified reactor design, and potential reductions in operating costs [9,10]. However, there are still challenges, particularly in scaling up the process and developing robust materials that can both withstand the conditions and efficiently convert the magnetic energy into heat.

Magnetic nanoparticles based on iron oxide, such as magnetite (Fe_3O_4), are commonly used in magnetically heated catalysis due to their simple synthesis, made from inexpensive starting materials, and exhibit excellent heating efficiency [10–12]. Magnetite is particularly attractive for ammonia synthesis, as the conventional industrial catalyst is also iron-based [13]. However, under reducing conditions, magnetite can partially transform into paramagnetic wüstite (FeO) even at room temperature, leading to a significant loss of the magnetic properties essential for magnetically induced heating [14,15]. To overcome this limitation, Almind et al. [16] developed a cobalt–nickel-based catalyst that maintained stable magnetic properties during steam reforming of methane. The alloy nanoparticles exhibited high Curie temperatures of 617 to 921 °C, highlighting their potential as effective susceptors for ammonia synthesis under magnetically heated conditions.

Motivated by recent advances in magnetically heated catalysis, we have developed and synthesised a completely new type of nanocomposite catalyst - spherical nanoparticles made of a $Co_{0.67}Ni_{0.33}$ alloy, uniformly coated with γ-Al_2O_3 nanosheets, using a customised protocol that allows precise control of the nanoparticles-to-support ratio and can be easily adapted to other supports [17]. We further decorated this nanocomposite with Ru nanoparticles and promoted it with Ba to enhance activity. In this study, we demonstrate for the first time an electrified ammonia synthesis reaction by magnetic heating - a reaction pathway not previously realized. To enable this, we have also developed a custom reactor system specifically designed for magnetically drives catalysis, allowing fast "on"/"off" switching of NH_3 synthesis within 2 to 3 min, simply by applying or removing an AMF. Furthermore, our theoretical calculations indicate that Ba promotion provides a synergistic enhancement of active Ru sites that extends beyond classical electrostatic interactions.

2. Materials and methods

2.1. Materials

Cobalt (II) Nitrate Hexahydrate, 98.0–102.0%, LOT: C24U002, Alfa Aesar; Nickel (II) Nitrate Hexahydrate, ≥ 97.0%, LOT: MKCM2708, Sigma-Aldrich; Sodium Hydroxide – pellets, 98.96%, LOT: 1911325, Fisher Chemical; Sodium Hypochlorite, < 60 g of active chlorine per L, TKI Hrastnik; Aluminium Nitride, Grade C, H.C. Starck; Ruthenium (III) Chloride Hydrate, 99.98% trace metals basis, Sigma-Aldrich; Barium Nitrate, 99 + %, Chemlab.

2.2. Synthesis of the magnetic catalyst (Ba-Ru/CN-A)

2.2.1. The magnetic support (CN-A)

The magnetic support (CN-A) was synthesised according to our previously described procedure [17]. Briefly, the synthesis was performed in the following steps: Aqueous solutions of Co^{2+} and Ni^{2+} were co-precipitated to achieve a composition of 67 wt% Co / 33 wt% Ni. The resulting hydroxide precipitate was immediately coated in situ with boehmite (AlOOH) nanosheets by controlled AlN hydrolysis [18]. The wet composite was freeze-dried and then reduced under a continuous stream of H_2 at 850 °C for 1 h. During this treatment, the CoNi hydroxides transform into $Co_{0.67}Ni_{0.33}$ alloy nanoparticles and the AlOOH shell dehydrates to γ-Al_2O_3, resulting in a 50:50 (*w*/w) CoNi / Al_2O_3 nanocomposite (CN-A).

2.2.2. Deposition of Ru nanoparticles (Ru/CN-A)

Prior to deposition, CN-A was repeatedly washed to remove residual chlorides and then redispersed in water (10 mg mL^{-1}). With vigorous stirring, a Ru^{3+} stock solution and 1 M NaOH were added alternately to maintain a pH of 9 so that nominally 1 wt% Ru was deposited on the support. The solid was freeze-dried and reduced at 500 °C for 2 h to obtain Ru/CN-A.

2.2.3. Barium promotion (Ba-Ru/CN-A)

A barium nitrate solution (3.4 mg mL^{-1}) was added to 300 mg Ru/CN-A and the mixture was sonicated for 20 min. After removal of the solvent by rotary evaporation, the powder was reduced at 500 °C for 1 h, yielding Ba-Ru/CN-A with a nominal Ba loading of 4.5 wt%.

2.3. Catalyst characterization

XRD: A PANalytical Empyrean diffractometer in Bragg-Brentano geometry (Cu Kα radiation) was used for the powder X-ray diffraction (XRD) analysis at room temperature. XRD patterns were recorded in the 2θ range from 10° to 70°, with a measurement step of 0.066° and a step time of 800 s (equivalent for point detector).

STEM: A transmission electron microscope (TEM) Jeol JEM 2010F operated at 200 kV and Cs-probe corrected scanning-transmission electron microscopes (STEM) Jeol ARM 200CF STEM operated at 80 kV and Thermo Fisher Scientific Spectra 300 operated at 200 kV were used for the (micro)structural characterization. A suspension of sample powders was deposited on a copper-grid-supported lacy carbon foil and left to dry naturally at room temperature. During the STEM analysis, HAADF and BF detectors were used simultaneously at 68–180 and 10–16 mrad collection semi-angles, respectively. The chemical composition of the samples was analysed in the STEM using a Jeol Centurio EDXS system with a 100 mm^2 SDD detector. The particle size distributions are presented as equivalent diameters for at least 124 individual particles, such that the diameter of a circle having equal surface area to the imaged particle.

BET: The surface properties were determined from nitrogen adsorption/desorption isotherms measured for samples at liquid-nitrogen temperature using a Nova2000e (Quantachrome Instruments Version 11.05, Boynton Beach Florida) nitrogen-sorption analyser. Prior to the measurements the samples were degassed over night at 120 °C in a vacuum. The surface area was calculated using the Brunauer-Emmet-Teller (BET) equation with nitrogen-adsorption data in the P/P_0 range between 0.005 and 0.3 (14-point analysis). The pore size and pore volumes were obtained using the Barrett–Joyner–Halenda (BJH) model from the desorption curve of the isotherms.

VSM: The room-temperature magnetization curves were measured with a Lakeshore Cryotronic Series 8600 VSM.

Calorimetric measurements and SAR values: Specific absorption rate (SAR) measurements were conducted in a hydrogen atmosphere under various temperatures and magnetic field conditions. The experimental setup, methodology, and data analysis are described in the ESI (Fig. S31–35, Table S6–7).

XPS: Spectra were collected using the PHI VersaProbe 3 AD (Phi, Chanhassen, US) using a monochromatic Al Kα X-ray source. For charge neutralisation, the charge of the sample was attenuated with two beams (electrons and ions). The peak shift caused by the neutralisation was corrected by shifting the peaks of the adventitious carbon species to 284.8 eV. The survey spectra were measured at a transit energy of 224 eV with a step of 0.8 eV, while the high-resolution spectra were measured at a transit energy of 27 eV and a step size of 0.05 eV. For the survey spectra, 2 sweeps were made, while for the high-resolution spectra, there were 25 sweeps performed. Spectral deconvolution was made using Kherve software.

NH_3-TPD: Acidity of the magnetic catalysts was analysed using NH_3 temperature programmed desorption (NH_3-TPD). Experiments were performed on a Microtrac Belcat II Chemisorption Analyser

(MicrotracBEL Corp., Osaka, Japan). The sample was positioned inside a quartz reactor and pre-treated in a flow of 5.05% H_2/Ar at 500 °C for 1 h. After pre-treatment, it was cooled to 100 °C in Ar and saturated with 9.87% NH_3/He for 20 min. Weakly absorbed NH_3 was removed in a flow of Ar for 30 min. The samples were heated to 500 °C at 10 °C min^{-1} and NH_3 desorption was a mass spectrometer (BelMass) following the characteristic $m/z = 15$ fragment. Acid sites were calculated based on known response of calibration gas mixtures.

CO-PA: The presence of metallic sites on the surface of catalysts was assessed using CO pulsed adsorption (CO-PA). The experiment was conducted on the chemisorption analyser mentioned above. The sample (approx. 50 mg) was positions inside a quartz reactor and pre-treated in a flow of 5.05% H_2/Ar at 500 °C for 1 h. After cooling to −10 °C in Ar, CO pulses were gradually increased until saturation. The total amount of adsorbed CO was determined by integrating the signal corresponding to the characteristic $m/z = 28$ fragment detected by the mass spectrometer.

2.4. Catalyst testing

Schematic illustration of reactor used for magnetically heated reactions is presented in Fig. S1. An induction coil (Ultraflex HS-4W resonant circuit featuring 0.66 μF capacitors coupled with a 9-turn flat-wound copper tube, 17-mm inner diameter, 29-mm outer diameter, 56-mm height operating at a constant 234 kHz) powered by the corresponding SHT-2/400 power supply was positioned around a fixed-bed quartz reactor tube (6-mm inner diameter, 360-mm length). For safety reasons, the quartz reactor tube was mounted within a stainless-steel pressure housing and enclosed in a protective containment box to mitigate risks associated with high-pressure operation. The magnetic field amplitude and frequency were measured by a custom-made probe assembly placed in the centre of the induction coil. An N-type thermocouple was inserted approximately into the middle of the material by height. The temperature of the catalyst bed (T_bed) was continuously monitored using a Tenma thermometer and the induction heater's power adjusted accordingly to maintain the desired temperature. The temperatures measured by the N-type thermocouple itself at different magnetic field strengths are presented in Fig. S2. A recirculating cooler from Julabo (FL1701) was used to circulate chilled water through the copper coil.

2.4.1. Ammonia synthesis experiments using magnetic heating

2.4.1.1. Steady-state operation at a constant thermocouple-measured bed temperature. The catalytic experiments were performed in a custom designed fixed-bed reactor compatible with magnetic heating. About 150 mg of material was fixed in a quartz tube between quartz wool plugs. The material was pre-treated in a flow of hydrogen (20 mL min^{-1}) at 400 °C for 1 h (corresponding to approx. 25 mT) to ensure complete reduction of the material. The ammonia synthesis reaction was performed at 3 and 5.5 MPa, and in the temperature range between 250 and 600 °C. The ratio of reactants H_2:N_2 was 2. The gasses were introduced into the reactor with mass flow controllers (BROOKS SLA5850) from cylinders with pure nitrogen and hydrogen gas (Messer, 5.0). The total gas flow was fixed at 60 mL min^{-1} (WHSV: 24000 mL g^{-1} h^{-1}) confirmed with mass a flow meter (ADM Flow Meter, Agilent).

Under the selected conditions (5.5 MPa, H_2:N_2 = 2:1, total flow rate of 60 mL min^{-1}, 150 mg catalyst), stability tests were performed at 600 °C for Ru/CN-A and at 400 °C for Ba-Ru/CN-A. The stability test for Ru/CN-A lasted 90 h, while the test for Ba-Ru/CN-A was carried out for 120 h.

2.4.1.2. Dynamic conditions. Under the selected conditions (5.5 MPa, H_2:N_2 = 2:1, 60 mL min^{-1}, 150 mg catalyst), dynamic experiments were carried out at 600 °C for Ru/CN-A and at 400 °C for Ba-Ru/CN-A. In the dynamic experiments, the alternating magnetic field (AMF) was switched on and off periodically, which led to heating and cooling of the reaction mixture. The switch-on and switch-off intervals were determined on the basis of reaching a steady state. The reproducibility was checked by several consecutive cycles.

2.4.2. Ammonia decomposition experiments using magnetic heating

2.4.2.1. Steady-state operation at a constant thermocouple-measured bed temperature (T_bed). Ammonia decomposition was conducted in the same reactor and with the same catalyst as the one we used for ammonia synthesis. Briefly, approximately 150 mg of Ba-Ru/CN-A, fixed within the quartz reactor, was pre-reduced at 400 °C for 1 h under a flow of H_2 at 30 mL min^{-1} to remove potential oxide species. The decomposition of pure NH_3 (Messer, ≥ 99.5%) at a flow rate of 66 mL min^{-1}, (confirmed with a glass bubble flow meter) was carried out from 500 °C down to 230 °C.

The stability test for the Ba-Ru/CN-A was carried out at 425 °C. The NH_3 flow rate through the reactor was maintained at 18 mL min^{-1}, and the gas downstream was diluted with He at a flow rate of 48 mL min^{-1}. The stability test for Ba-Ru/CN-A lasted 120 h.

2.4.2.2. Dynamic conditions. The dynamic experiment for Ba-Ru/CN-A (150 mg) was conducted at 400 °C. The NH_3 flow rate through the reactor was 18 mL min^{-1}, and the outlet stream was diluted with He at 48 mL min^{-1}. In the dynamic test, the AMF was switched on and off at regular intervals, resulting in heating and cooling of the reaction mixture. The duration of each switch-on and switch-off cycle was determined on the basis of reaching a steady state. Repeatability was confirmed by multiple consecutive cycles.

2.4.3. Experiments using external thermal heating

Both the ammonia synthesis and the cracking were also carried out under external thermal heating conditions, referring to laboratory-scale heating provided by an external furnace or cartridge heater, as opposed to industrial adiabatic reactor operation. The same reactor setup was used, with the copper coil being replaced by a custom-designed reactor heated by heating cartridges in an aluminium block.

2.5. Product analysis

The concentration of effluents was analysed by an on-line gas chromatography (Inficon Micro GC Fusion Gas Analyser) by the separation on PLOT (Rt-Q-BOND) and Rt-MolSieve 5 A (MS5A) columns and quantified by a TCD detector. The concentration of effluents in the dynamic experiments was monitored using a portable mass spectrometer (QMS200 Standford Research Systems), monitoring the signal for H_2 (2), NH_3 (16), NH_3 (17), H_2O (18), N_2 (28) and O_2 (32). After testing, the spent catalyst was cooled in a nitrogen flow and stored under argon for further analysis.

2.6. Ab initio calculations

First principles calculations were performed at the density functional theory level in the plane-wave approach, as implemented in VASP [19–21]. To describe electronic interactions, the Perdew-Burke-Ernzerhof (PBE) functional was used [22,23], which exhibits a good compromise between the computational cost and accuracy, especially for metallic systems. An energy cut-off of 400 eV sufficed for well converged results, while a Gaussian smearing of 0.05 eV was employed for easier convergence. A Γ-centred K-point mesh of 3x3x1 was used for slab calculations and a Γ point sampling for isolated species. To compensate for a poor description of the dispersion interactions, the Grimme D3 correction was used [24]. For slab calculations, the dipole correction in the z direction was turned on, while for vacuum calculation the correction was applied in all directions [25]. Geometry relaxation of

the structures was deemed complete when the individual forces on atoms dropped below 0.01 eV/Å. The transition states were identified using the dimer method [26,27] and confirmed with the vibrational analysis to contain one imaginary frequency.

The system of active ruthenium with barium doping was modelled, as described by Baik et al. [28], and geometrically reoptimized with the parameters used in our work. The model incorporates a Ru_{13} cluster, deposited in the lowest-energy position on a 2 × 2 supercell of BaO with 4 layers. The bottom two layers are frozen in their bulk positions. To ascertain the effect of the support and decouple it from the geometry effect, the same geometry of Ru_{13} was used as an isolated cluster, as well. When the effect of the electronic charge was probed, the compensating background charge (jellium) was spread around the cluster to ensure electroneutrality of the periodic cell.

Adsorption energy of N_2 was calculated as

$$E_{ads} = E_{N2/cat} - E_{cat} - E_{N2} \tag{1}$$

where $E_{N2/cat}$ is the energy of the system with adsorbed N_2, E_{cat} is the energy of an empty catalyst surface and E_{N2} is the energy of an isolated molecule of N_2. Analogously, the reaction energy is defined as

$$\Delta E_r = E_{N+N/cat} - E_{N2/cat} \tag{2}$$

and the activation barrier as

$$E_{A,LH} = E_{TS} - E_{N2/cat} \tag{3}$$

where E_{TS} is the energy of transition state for N_2 dissociation. In this case, the Langmuir-Hinshelwood mechanism is assumed, i.e. N_2 first adsorbing. Especially when the initial interaction is weak, the Eley-Rideal is also possible, where we have

$$E_{A,ER} = E_{TS} - E_{cat} - E_{N2} \tag{4}$$

The two are connected, as follows

$$E_{A,LH} + E_{ads} = E_{A,ER} \tag{5}$$

2.7. Microkinetic modelling

The reaction rate and the total species consumption/generation were computed as shown below.

$$r_n = k_{forward} \prod_{i=1}^{I} \theta_i^{S_{i,n,forward}} - k_{backward} \prod_{j=1}^{I} \theta_j^{S_{j,n,backward}} \tag{6}$$

$$\frac{d\theta_i}{dt} = R_i = \sum_{n=1}^{N} \left(-S_{i,n,forward} + S_{i,n,backward} \right) r_n \tag{7}$$

We assume site balance:

$$1 = \theta_* + \theta_\# \tag{8}$$

r_n represents the rate of the n-th reaction, while $k_{forward}$ and $k_{reverse}$ are the forward and reverse reaction rate constants, respectively. θi denotes the surface coverage of species i (dimensionless), and $S_{i,n,forward}$ and $S_{i,n,reverse}$ are the stoichiometric coefficients of species i in the forward and reverse reactions. I and N represent the number of species and reactions, respectively. * are RuBa sites for N_2 activation and # are Ru sites for H_2 activation. For adsorption reactions following expression was used:

$$r_{ads} = k_{forward}\, p_i \theta_g \tag{9}$$

where *g* represents free active sites (*,#). Desorption reactions are given in the same manner as other surface reactions. For the reactor transport model, two different models were compared: Ideally mixed continuous stirred-tank reactor (CSTR) and temperature distribution CSTR model. The overall mass balance equations for both reactor types are shown below (Eq. (10)).

$$\text{CSTR}: \quad \frac{dC_i}{dt} = \frac{v_{ax.}}{L}\left(C_{i,inlet} - C_i\right) + c_g\, \rho_{cat} \frac{1-\varepsilon}{\varepsilon} R_i \tag{10}$$

Here, *t* represents the time dimensions of the reactor while i denotes the species. v_{ax} is the superficial gas velocity in the axial (lengthwise) direction of the reactor, and L is the reactor length. C_i and $C_{i,inlet}$ are the gas-phase and inlet concentrations of species i, respectively, while R_i is the sum of all reaction terms for species i. ϵ is the void fraction, assumed to be 0.4. C_g represents the concentration of active sites per mass of the catalyst and ρ_{cat} is bed density. The constants are given in following expression (Eq. (11)).

$$k = AT^n e^{-\frac{Ea}{RT}} \tag{11}$$

The modelling was performed using Python using continuously stirred tank reactor model. The model was solved using solve ivp function, by implementing LSODA solver including Jacobian. We upgraded initial CSTR model with temperature distribution factor, since it includes the most important contribution to the description of this magnetic heated reactor. Further information is given in ESI (including determination of apparent reaction orders, activation energies and coverages and temperature distribution incorporation, Table S1–5, Fig. S11–30).

3. Results and discussion

3.1. Catalyst characterization

Magnetic heating-assisted ammonia synthesis requires the development of an efficient magnetic catalyst. The magnetic catalyst support was synthesised in this study according to our previously established procedure [17]. It consists of ferromagnetic CoNi alloy nanoparticles embedded within an Al_2O_3 matrix (CN-A). In addition, ruthenium was deposited on the surface (Ru/CN-A) and further promoted with barium oxide (Ba-Ru/CN-A). The XRD pattern of the final nanocomposite Ba-Ru/CN-A (Fig. S3a) displays broad reflections characteristic of small tetragonal γ-Al_2O_3 crystallites alongside narrower peaks at d-spacings matching fcc CoNi alloy (a = 3.546 Å). STEM imaging (Fig. 1) revealed a hierarchical nanostructure of Ba-Ru/CN-A. The globular CoNi NPs with a size of 25.6 ± 8 nm were homogeneously covered with nanostructured shell of small-alumina crystallites (3–5 nm thick, several tens of nm wide). Individual, globular Ru NPs (2–7 nm in size) were scarcely distributed over the alumina surfaces (marked with red circles in Fig. 1b). In addition, bright dots are visible on the atomic-resolution HAADF images of thin alumina nanosheets that can be assigned to Ba promoters (EDS mapping, Fig. S4 and Fig. S5). Nitrogen adsorption–desorption isotherms (Fig. S3b) classify CN-A as mesoporous (type IV) with 5–50 nm pores and a BET surface area of 110 $m^2\ g^{-1}$. The room-temperature magnetization curves of CN-A, Ru/CN-A and Ba-Ru/CN-A (Fig. 2a) confirmed soft ferromagnetic properties with a narrow hysteresis loop. The reduction in saturation magnetization observed for the Ru- and Ru/BaO-functionalized samples can be partly attributed to the dilution effect caused by the deposition of non-magnetic phases onto the CoNi alloy. However, the observed decrease is greater than what would be expected from mass dilution alone, suggesting that partial oxidation of the CoNi nanoparticles during impregnation and air exposure leads to the formation of surface oxide layers, which further reduce the effective ferromagnetic volume. The Curie temperature exceeded 900 °C (Fig. S3c), underscoring the material's suitability for high-temperature magnetic heating applications. The total heating effect of the CN alloy nanoparticles was estimated using a custom calorimetric device coupled with an induction heater. The effects were determined as a function of the applied magnetic field, consequentially, the temperature of the sample. The total heating effect, produced by the alternating magnetic field, for the ensemble of magnetic nanoparticles was found to increase with the temperature of the sample from 3.0 W g^{-1} at 100 °C up to 3.9 W

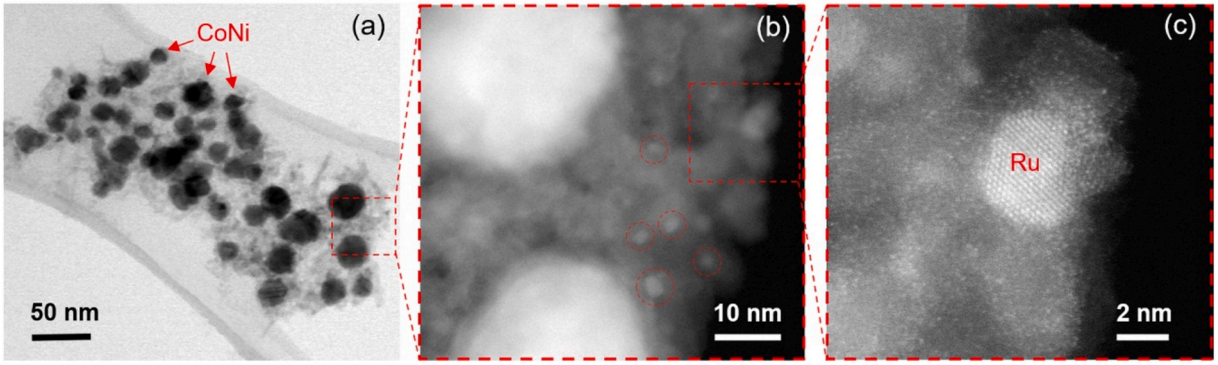

Fig. 1. (a) BF and ((b) and (c)) HAADF STEM images of magnetic catalyst Ba-Ru/CN-A taken at increasing magnification.

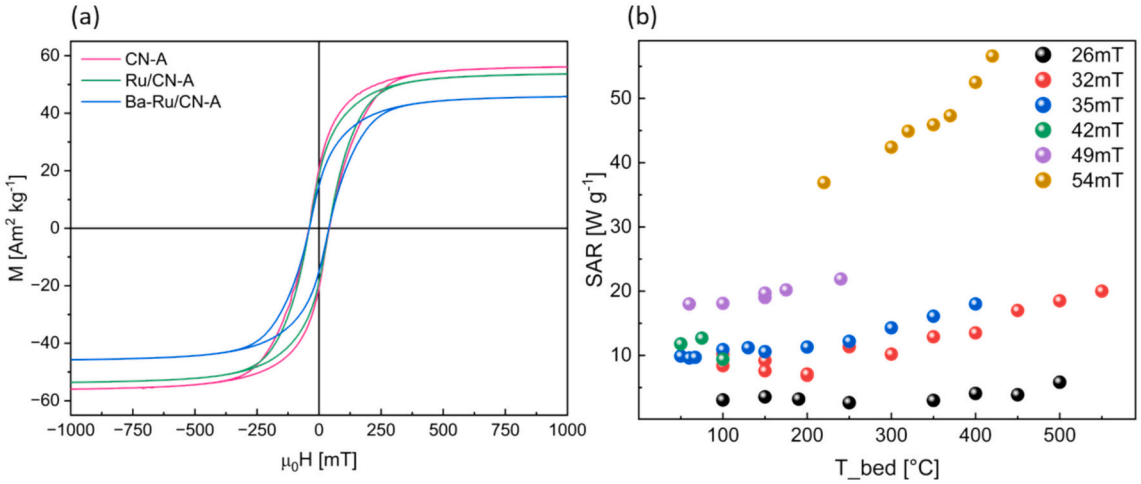

Fig. 2. (a) Room-temperature magnetization curve of CN-A, Ru/CN-A and Ba-Ru/CN-A and (b) magnetic heating effect (SAR) of CN-A depending from temperature (T_bed) at various applied altering magnetic field (f = 234 kHz). All temperatures refer to thermocouple-measured catalyst bed temperatures (T_bed).

g^{-1} at 450 °C at 26 mT (black dots in Fig. 2b, Fig. S32).

XPS was performed on fresh catalysts to determine the surface species present on the catalyst surface before the reaction. As already noted in our previous publication [17], the Ni and Co regions exhibit very complex structures where several oxide species cover a metallic core of the particles (Fig. S7 and S8). In the case of promotion with Ba, additional complexity is introduced due to overlaps with the Co region. In all cases Ru analysis was impossible, as all the peaks overlap with other elements present in the material. Cleaning the surface with Ar^+ was not performed, as this could affect the oxidation state of the surface bound species. The Ba 4d region exhibits a standard doublet expected from an oxidized Ba species (Fig. 3). The position of the first peak (89.6 eV) indicate that, most likely, Ba is present in the form of $Ba(OH)_2$ [29], which is consistent with what one would expect with the synthesis technique employed.

Pulsed CO chemisorption (CO-PA) measurements were performed to quantify the accessible metallic sites on the catalyst surfaces (Table 1). The CN-A support adsorbed 83.3 μmol CO g^{-1}, indicating that a significant portion of the Co and Ni sites remain accessible despite encapsulation by γ-Al_2O_3 nanosheets. After the deposition of Ru, the total CO uptake increased significantly. By subtracting the CO adsorption attributable to Co and Ni (as measured for CN-A), the Ru-specific CO uptake for Ru/CN-A was determined to be 43.3 μmol g^{-1}. X-ray fluorescence analysis (XRF) revealed a Ru content of 0.81 wt%, corresponding to 80.14 μmol of total Ru per gram of the catalyst. These values result in a Ru dispersion of 54%, which corresponds to an estimated average particle size of about 2.3 nm, assuming a spherical geometry and uniform distribution. The introduction of Ba as a promoter led to a

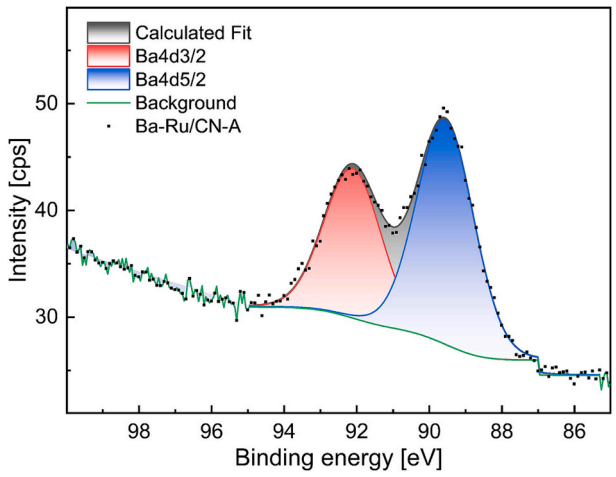

Fig. 3. High-resolution XPS spectra of the Ba 4d region for the Ba-Ru/CN-A catalyst. The spectrum shows the characteristic Ba 4d doublet, with the $4d_{5/2}$ component located at 89.6 eV and the $4d_{3/2}$ component at 92.1 eV, consistent with Ba in an oxidized surface environment.

decrease in the concentration of exposed metallic sites, indicating a partial coverage of the active sites by Ba species. This observation indicates that Ba is probably present in the Ba^{2+} oxidation state, which is consistent with its low ionization energy and high reactivity. Assuming equal relative coverage of CoNi and Ru sites, the estimated Ru surface

Table 1
Ammonia adsorption capacity, concentration of acidic sites, area ratio of low- to high-temperature NH_3 desorption peaks, and surface metallic site density (as determined by CO pulse adsorption) for CN-A, Ru/CN-A, and Ba-Ru/CN-A catalysts.

Sample	Volume of NH_3	Conc. of acidic sites	Area ratio	Conc. of metallic sites
	[mL g_{cat}^{-1}]	[μmol g_{cat}^{-1}]	low/high T peak	[μmol g_{cat}^{-1}]
CN-A	0.560	19.3	0.5/0.5	83.3
Ru/CN-A	1.298	52.5	0.2/0.8	126.6
Ba-Ru/CN-A	0.665	26.7	0.4/0.6	60.4

coverage by Ba is about 52%.

Temperature-programmed ammonia desorption (NH_3-TPD) was used to analyse the acidic properties of the catalysts, providing insights into both the strength and amount of the acidic sites. As shown in Fig. 4, the deconvoluted desorption profile shows two main NH_3 desorption peaks centered at around 200 °C and 274 °C. Although there are probably several adsorption sites, they can be roughly grouped into the two peaks mentioned above. After the deposition of Ru (Ru/CN-A), the proportion of high-temperature desorption sites increases significantly, shifting the area ratio between low and high-temperature peaks from ~50:50 to 17:83. Subsequent promotion with barium (Ba-Ru/CN-A) brings this ratio back to almost one (Table 1), indicating a redistribution of acid sites.

Decoration with Ru increases the total volume of adsorbed NH_3 by a factor of 2.3 compared to bare CN-A. Subsequent Ba deposition reduces this value to a level comparable to CN-A, indicating partial coverage of Ru sites by Ba. Interestingly, the NH_3 desorption peak for Ba-Ru/CN-A remains centered near 200 °C but is slightly shifted to higher temperatures, suggesting a more dynamic balance between NH_3 adsorption and desorption. According to the Sabatier principle, achieving this balance is crucial for optimal catalytic conversion. These results emphasize the synergistic effect of Ba promotion in modulating the ammonia adsorption properties of Ru/CN-A, which contributes to the improved catalytic performance of Ba-Ru/CN-A, partly by attenuating stronger NH_3 binding (vide infra).

3.2. Catalytic experiments

Ruthenium is a well-established second-generation catalyst for ammonia synthesis, known for its ability to cleave the robust N≡N bond and facilitate nitrogen adsorption. Typically, Ru is supported on various materials [30,31] and often promoted with alkali or alkaline earth metals [32–34]. These promoters fulfill several functions: They can anchor Ru nanoparticles [35], suppress migration and agglomeration [33] and modulate the electronic and adsorptive properties of the active sites.

Given the susceptibility of the $Co_{0.67}Ni_{0.33}$-Al_2O_3 (CN-A) support to oxidation, all catalysts were pre-reduced in a hydrogen atmosphere at 400 °C for 1 h prior to the catalytic tests. This treatment effectively restored the magnetic properties of the CoNi nanoparticles, as previously demonstrated [17].

Preliminary pressure-dependent ammonia synthesis experiments were performed using the Ru/CN-A catalyst as a representative catalyst. Based on these results, ammonia synthesis experiments were conducted at pressures of 3.0 MPa and above, as lower pressures resulted in very low single-pass ammonia yields (<0.6%), limiting the relevance of the data for meaningful catalytic and process-oriented evaluation (see Fig. S9). All subsequent catalytic evaluations were therefore performed at 5.5 MPa. As shown in Fig. 5, the unmodified CN-A support exhibited measurable ammonia synthesis activity at elevated temperatures (>500 °C) and achieved a yield of approximately 0.7% (2 mmol NH_3 g_{cat}^{-1} h^{-1}). This indicates that the surface-exposed Co and Ni sites are accessible to reactant gases. Deposition of less than 1 wt% Ru (Ru/CN-A) significantly improved the performance, increased the ammonia yield to over 1.2%, and lowering the temperature for peak activity by 50 °C. Further promotion with Ba (Ba–Ru/CN-A) did not noticeably increase the yield but shifted the temperature required for peak activity from 550 °C to 350 °C. These trends are consistent with the NH_3-TPD analyses, where Ba promotion resulted in lower desorption temperatures compared to Ru/CN-A, indicating facilitated ammonia desorption (Fig. 4). At higher temperatures, a decrease in ammonia yield was observed for all catalysts (Fig. 5), while the yields remain well below the thermodynamic equilibrium values, reflecting an inherent kinetic–thermodynamic trade-off that is more pronounced under magnetically heated operation. Although elevated effective temperatures enhance reaction kinetics, they simultaneously constrain equilibrium-limited single-pass yield. It should be noted that the temperatures reported here correspond to thermocouple-measured catalyst bed temperatures (T_bed) rather than the actual temperatures at the catalytically active sites.

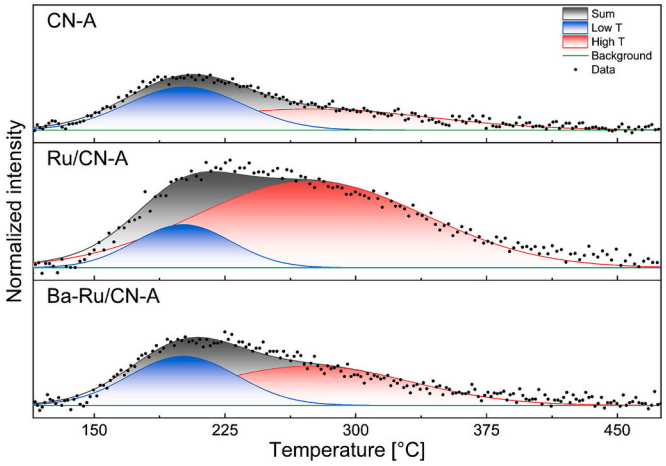

Fig. 4. Normalized NH_3-TPD curves of the fresh catalysts (CN-A, Ru/CN-A and Ba-Ru/CN-A).

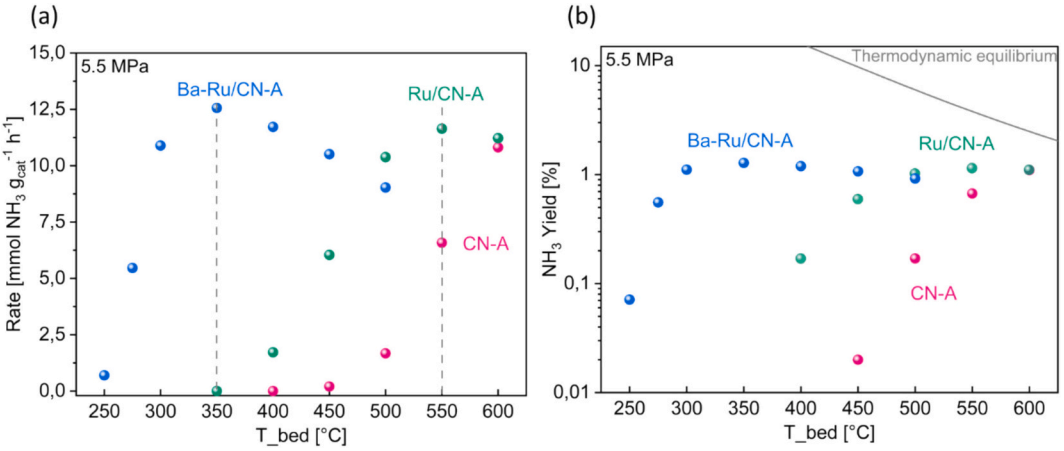

Fig. 5. (a) Reaction rate and (b) NH_3 yield as a function of catalyst bed temperature for CN-A, Ru/CN-A, and Ba-Ru/CN-A catalysts, measured under identical conditions (5.5 MPa, total gas flow of 60 mL min^{-1}, 234 kHz). All temperatures refer to thermocouple-measured catalyst bed temperatures (T_bed).

To evaluate the long-term stability, experiments were carried out for at least 90 h (Fig. 6a-b). The ammonia synthesis rates remained largely stable, with a negligible decrease observed. For the Ru/CN-A catalyst, an intentional interruption of the AMF was performed for about 5 h to evaluate possible deactivation mechanisms such as surface restructuring or fouling. After reactivation of the magnetic field, the reaction rate and temperature quickly returned to their previous steady-state values, indicating robust catalyst stability under dynamic operating conditions. STEM analysis of spent catalyst Ba-Ru/CN-A revealed no discernible changes in the size or morphology of the Ru nanoparticles or distribution of barium species. In contrast, the CoNi alloy nanoparticles exhibited an average growth of about 5 nm (Fig. S6); however, they maintained efficient magnetic heating performance.

Building on these findings, dynamic catalytic experiments (Fig. 6c-f) demonstrated the system's responsiveness, which is particularly relevant for integration with intermittent renewable energy sources. In these experiments, the magnetic field was periodically switched on and off while maintaining a constant reactant flow. The duration of each cycle was defined by the time required for the catalyst to reach more than 99% of its maximum activity, followed by a corresponding field-off period. The Ru/CN-A catalyst reached steady-state operation in less than 20 min, whereas the Ba–Ru/CN-A catalyst attained over 95% of its peak activity within only 10 min. These results demonstrate rapid and reversible activity modulation under magnetic heating. Although long-term cyclic (more than 10 cycles) operation was not investigated, stable performance during 120 h of continuous operation suggests that the catalyst is stable. Overall, findings highlight the fast thermal response and operational flexibility enabled by magnetic heating, underscoring its potential for on-demand ammonia production in renewable energy-driven processes.

To further assess the versatility of the catalyst in electrification and industrial decarbonisation, similar experiments were conducted with the Ba–Ru/CN-A catalyst for the decomposition of pure ammonia (Fig. S10). The Ba-promoted catalyst converted over 95% at 450 °C, with this high conversion remaining stable for 120 h (Fig. S10(a)). Dynamic tests showed that the catalyst reach steady-state conversion even faster during ammonia decomposition than during synthesis, which can be attributed to the lower pressure conditions. In addition, the catalyst demonstrated excellent stability over multiple consecutive on-and-off cycles of ammonia decomposition.

3.3. Mechanistic insight into Barium promotion

Experimental findings clearly show that the ammonia synthesis rate significantly increased from 158 to 1430 mmol NH_3 g_{Ru}^{-1} h^{-1} at 400 °C when Ba was added to the Ru/CN-A catalyst (Fig. 5). Ba was added as a nitrate while the catalyst was heat treated where nitrate decomposes to BaO species (Fig. 3) [36].

To understand the role of BaO, density functional theory calculations were performed. The effect of barium support was described using the model proposed by Baik et al. [28], where a Ru_{13} cluster is deposited on a BaO(001) surface. The authors have shown a significant charge transfer from BaO to Ru upon the dissociative adsorption of H. Initially, H_2 dissociates on Ru, resulting in an overall charge on the Ru—H cluster of $-0.708e_0$. Thermodynamically, it is more favourable for the *proton* to migrate to the O in BaO, which increases the excess negative charge on Ru to $-1.084e_0$. Similarly, the authors have shown that the adsorbed N_2 is strongly negatively charged on Ru ($-0.88e_0$).

However, the reaction rate is a kinetic phenomenon, determined by the barrier of the rate-determining step, which is known to be N_2 dissociation (Fig. 7a). Our calculations show that on Ru/BaO, the adsorption strength of N_2 is 1.06 eV. The dissociation barrier is 1.21 eV, and the overall reaction energy is −1.19 eV, rendering the reaction highly exothermic. Several sites on the cluster were tested, and the interface (see Fig. 7b) between Ru and BaO was seen to perform best (i.e., having the lowest activation barrier), as opposed to the top site on Ru (far away from BaO).

To understand the effect of Ru and BaO, these calculations were repeated on a Ru_{13} cluster of the same shape in a vacuum, revealing weaker adsorption (−0.74 eV), a higher dissociation barrier (1.96 eV), and an overall endothermic reaction (+0.30 eV). However, an isolated Ru cluster is not charged as there is no support to draw the charge from. Artificially increasing the negative charge on Ru_{13} from 0.0 to −1.0, as shown in Fig. 7b-d, led to an increase in the interaction strength with N_2 and a decrease in the barrier for its dissociation, as excess electron density is injected in the anti-bonding orbital of N_2. The effect, however, is roughly an order of magnitude smaller than on Ru/BaO. For instance, $q = -1.0$ decreases the barrier on Ru_{13} for merely 0.13 eV, while on Ru/BaO it is 0.76 eV lower. Similarly, the increase in the adsorption strength and exothermicity is much lower on a negatively charged Ru_{13} than on Ru/BaO.

The synergistic effect of Ru and BaO extends beyond a simple electron injection. Geometric effects can be ruled out since the Ru cluster was maintained in the same shape, and the reaction was observed on the same site. Instead, the increased reactivity is proposed to stem from the energetically favourable formation of Ru–BaO interfacial sites. This observation also explains why an optimal coverage [28] of Ba and Ru is necessary for maximum catalytic performance—the number of interface sites must be maximized.

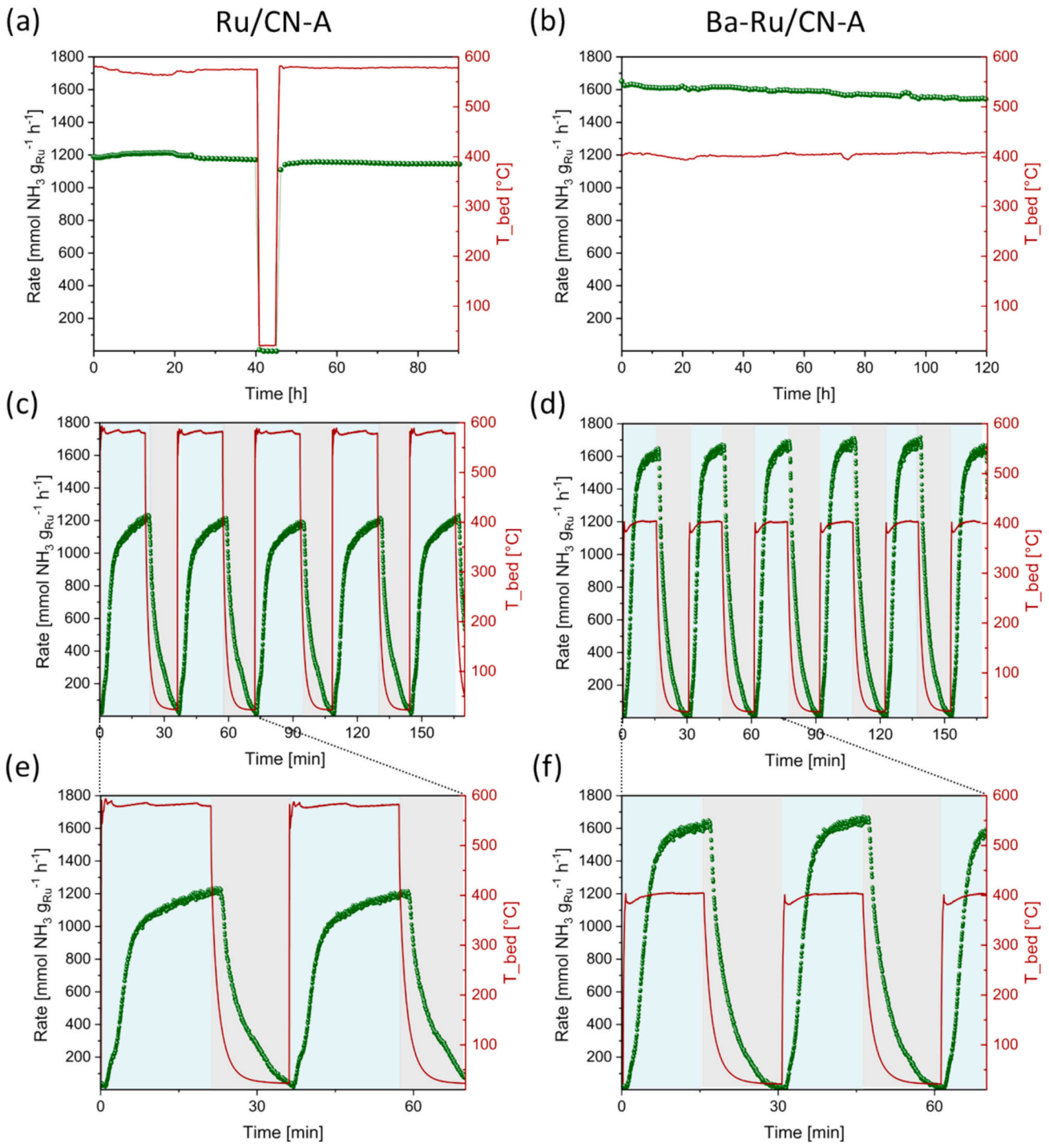

Fig. 6. Reaction rate as a function of time for (a, c, e) Ru/CN-A and (b, d, f) Ba-Ru/CN-A catalysts under (a, b) stable and (c, d) dynamic conditions. Conditions: 5.5 MPa, 60 mL min^{-1} total flow, H_2:N_2 = 2:1. Experiments were conducted at the respective temperatures of maximum activity—580 °C (~25 mT) for Ru/CN-A and 400 °C (~26 mT) for Ba-Ru/CN-A. Figures (c) and (d) show magnified views (0–75 min) of (a) and (b) to highlight steady-state behavior. All temperatures refer to thermocouple-measured catalyst bed temperatures (T_bed).

3.4. Reaction kinetics description

Based on our DFT analysis, we have developed a microkinetic model that includes different active sites: Ba—Ru interfaces (denoted as "*"), which are responsible for N_2 dissociation and N–H_x association, and Ru sites (denoted as "#"), which facilitate H_2 activated adsorption. To validate this approach, we analysed the structure–activity relationships. Baik et al. [28] innovatively demonstrated that H_2 treatment of BaRu and CsRu catalysts decreases CO_2 adsorption, which is due to the protonation of BaO and Cs_2O groups in contact with Ru, changing the basicity of the surface. A linear correlation was observed between the NH_3 synthesis activity and the difference in CO_2 adsorption capacity (after H_2

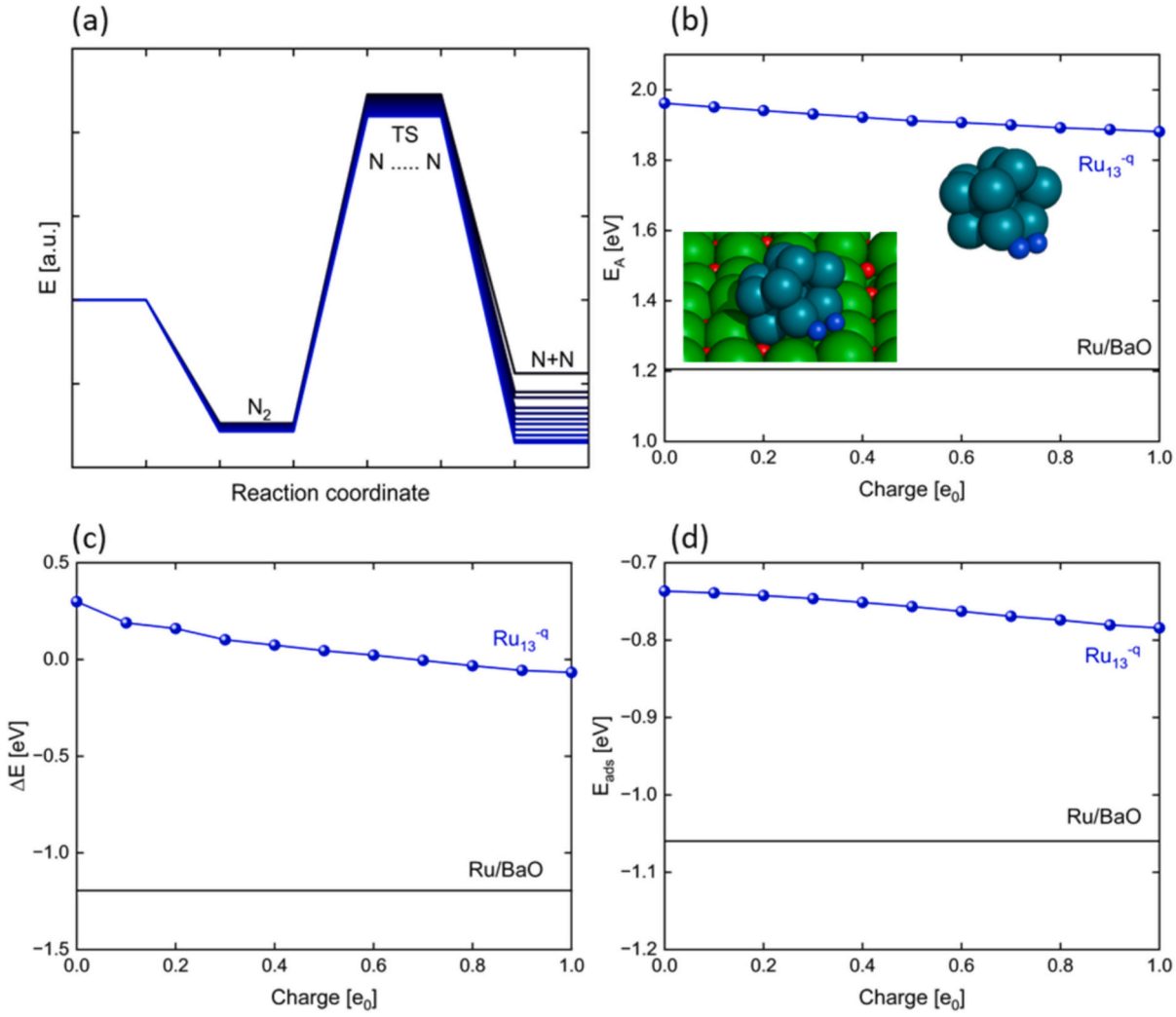

Fig. 7. (a) Potential energy surface for N_2 dissociation on a Ru_{13} cluster, as the overall charge on the cluster changes from 0.0 (black) to −1.0 e_0 (blue), and (b) activation energy, (c) reaction energy and (d) adsorption energy on the Ru_{13} cluster as a function of the overall charge on the cluster (blue line) and the values on the Ru/BaO structure.

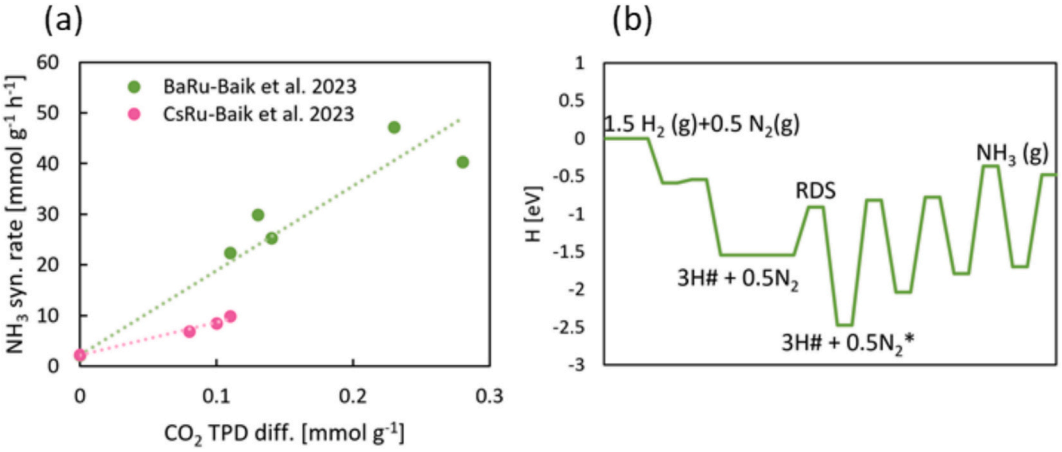

Fig. 8. (a) Structure-activity relations of for NH_3 synthesis rate, based on RuBa/RuCs intimate contact determined through CO_2 TPD difference of unreduced and reduced sample [28]. (b) Optimized energy diagram based on DFT calculations for N_2 activation on Ru-based surface.

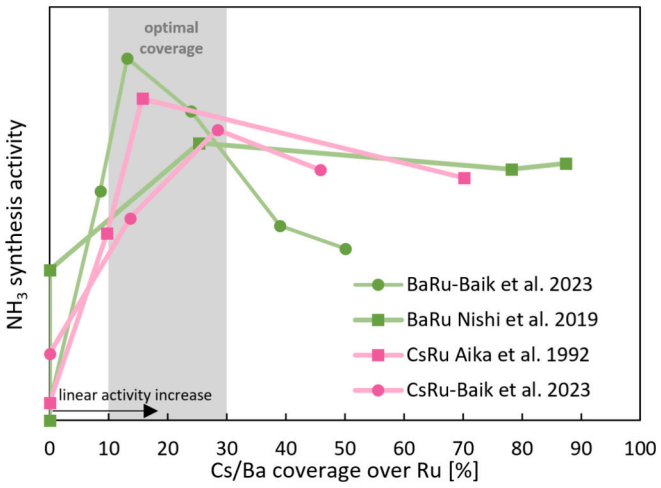

Fig. 9. The effect of coverage of Cs and Ba over Ru on the overall NH_3 synthesis activity.

treatment compared to inert gas treatment), which serves as an indicator of active Ba—Ru interfaces (Fig. 8a).

$$c_* = c_{CO\ PA}(Ru) - c_{CO\ PA}(RuBa)(\mathrm{N_2\ activation\ sites}) \quad (13)$$

$$c_\# = c_{CO\ PA}(RuBa)(\mathrm{H_2\ activation\ sites}) \quad (14)$$

If Ba coverage over Ru is above 20%:

$$c_* = c_{CO\ PA}(Ru) \times 0.2(\mathrm{N_2\ activation\ sites}) \quad (15)$$

$$c_\# = c_{CO\ PA}(RuBa)(\mathrm{H_2\ activation\ sites}) \quad (16)$$

To develop a two-site microkinetic model, we used DFT-derived energy profiles for NH_3 synthesis and decomposition on Ru(0001) and fitted them to the experimental observations (Fig. 8b). Remarkably, the incorporation of Ba into Ru significantly reduced the NH_3 binding energy - from about 160 kJ mol^{-1} (determined by Redhead analysis) [37] to below 80 kJ mol^{-1}, as evidenced by our NH_3-TPD measurements (Fig. 4). In agreement with previous findings of reduced CO adsorption, H_2 adsorption also decreased [28], with the addition of Ba. Assuming exclusive hydrogen adsorption on Ru, the desorption energy was calculated to be 113 kJ mol^{-1}, consistent with literature values (~125 kJ mol^{-1}) [38]. As for nitrogen activation, the Ru steps exhibit an N_2 activation energy of 37 kJ mol^{-1} and an N—N association energy [39] of 145 kJ mol^{-1}. For BaRu, we used N_2 activation energy of 42 kJ mol^{-1} and 119 kJ mol^{-1} for reverse reaction.

$$R(NH_3) = \frac{0.5 \cdot k_3 \cdot \frac{k_{2f}}{k_{2b}} \left(p(N_2) - \frac{p(NH_3)^2}{p(H_2)^3 \cdot Kp} \right)}{\left(1 + \frac{k_{4b}}{k_{4f}} \frac{k_{5b}}{k_{5f}} \frac{k_{6b}}{k_{6f}} \frac{k_{7b}}{k_{7f}} \cdot \frac{p(NH_3)}{\left(\frac{k_{0f}}{k_{0b}} \frac{k_{1f}}{k_{1b}} p(H_2) \right)^{3/2}} + \frac{k_{5b}}{k_{5f}} \frac{k_{6b}}{k_{6f}} \frac{k_{7b}}{k_{7f}} \cdot \frac{p(NH_3)}{\frac{k_{0f}}{k_{0b}} \frac{k_{1f}}{k_{1b}} p(H_2)} + \frac{k_{6b}}{k_{6f}} \frac{k_{7b}}{k_{7f}} \cdot \frac{p(NH_3)}{\left(\frac{k_{0f}}{k_{0b}} \frac{k_{1f}}{k_{1b}} p(H_2) \right)^{1/2}} + \frac{k_{7b}}{k_{7f}} p(NH_3) \right)^2} \quad (12)$$

NH_3 synthesis activity increased with Ba coverage on Ru, peaking at between 10 and 30% (Fig. 9), followed by a gradual decrease at higher coverages. Three possible factors were considered: (1) decreased H_2 activation, (2) decreased number of active Ba—Ru sites, and (3) decreased intrinsic activity of these sites. Given the negligible activation energy for H_2 activation (~3 kJ mol^{-1}), the first factor is unlikely. As for the second factor, a uniform Ba distribution would indicate a maximum formation of the active sites at 50% coverage (Fig. S11), which was not observed. Moreover, such configurations are not thermally stable due to the immiscibility of Ba and Ru (Fig. 1 and Fig. S5.). A more plausible scenario is the overgrowth of $BaO_{1-x}(OH)_x$ from the base of the Ru nanoparticles, leading to suboptimal interface exposure at higher coverages (Fig. S11). This trend was the same for all Cs-promoted systems. In this case, a partial agreement was observed between Ba/Cs coverage over Ru and a number of active sites.

The third factor is supported by experimental measurements of the apparent activation energy through the Arrhenius relation: It decreases from 93 kJ mol^{-1} (bare Ru) to 64 kJ mol^{-1} at 13% Ba coverage and then increases to over 80 kJ mol^{-1} at 50% coverage, although at 50% coverage the activity is much higher compared to unpromoted material (Fig. S11) relating to negligible pure Ru contribution to NH_3 synthesis [28]. This indicates that highly dispersed $BaO_{1-x}(OH)_x$ or smaller clusters increase the activity, while larger crystalline clusters weaken the promoting effect. Therefore, the intrinsic activity of Ba—Ru sites decreases at higher Ba coverages, limiting the model's applicability. Overall, based on these findings, we propose a straightforward approach to determine the active sites (based on Fig. 9):

If Ba coverage over Ru is below 20%:

The original DFT model was refined using data from experiments conducted under external thermal heating (including tests with CN-A–Ru–Ba for both synthesis and decomposition) and supplemented with literature data [40]. Comparative analyses revealed that the Ba—Ru catalyst exhibited higher activity in NH_3 decomposition than Ru alone, confirming literature reports [41]. Subsequent sensitivity analyses identified N—N dissociation and association as the rate-determining steps for NH_3 synthesis and NH_3 decomposition, respectively. The two-site model was further simplified to derive a generalised lumped kinetic expression that applies to both processes (1) and shows good agreement with experimental data (Fig. 10c). Furthermore, calculated apparent reaction orders presented in Fig. S17-S21 (NH_3 synthesis, H_2: ≈0, N_2: ≈0.6, NH_3: ≈ − 0.7), and apparent activation energies (NH_3 synthesis: ≈45 kJ mol^{-1}, NH_3 decomposition: ≈110 kJ mol^{-1}), closely correlates with literature values for NH_3 synthesis [28] and NH_3 decomposition [42]. In addition, full microkinetic model indicates (Fig. S22-S23), that Ru sites (#) are mostly occupied by H during NH_3 synthesis and decomposition, while RuBa sites (*) are almost completely occupied by N during decomposition below 500 °C and empty during NH_3 synthesis at 10 bar. Overall, the Ba—Ru two-site microkinetic model was validated based on DFT calculations and simplified for efficient computational application.

The direct magnetic heating of the catalyst has pronounced effects on the effective reaction temperature. First, the apparent reaction temperature under magnetic heating is more than 100 °C higher than the temperature measured with a thermocouple in the catalyst bed (T_bed). Consequently, the reaction locally approaches thermodynamic equilibrium more closely than suggested by the bed temperature alone, providing a consistent explanation for the observed relationship between high reaction rates and comparatively low single-pass ammonia

yields discussed above (Fig. 5). This temperature difference was determined independently using two complementary approaches, namely calorimetric measurements and extrapolation from kinetic simulations (see ESI), which yielded very similar estimates. Additionally, temperature gradients arise due to the varying distances between the heat source (CN alloy nanoparticles) and the active reaction sites. Fig. 10a-b compare the experimental results with kinetic models assuming uniform temperature and with models incorporating local temperature deviations (see ESI for details).

4. Discussion

When evaluating the ammonia synthesis performance (Table 2, Fig. 10d) of our Ba-promoted Ru/CN-A catalysts, the NH_3 synthesis rates normalized to catalyst mass are comparable to those reported in the literature for Ba- or Cs-promoted Ru catalysts supported on different oxide materials. Notably, direct magnetic heating was employed in the present study, in contrast to the external thermal heating methods used in previous reports. Reported values typically range from 0.15 to 60.2 mmol NH_3 g_{cat}^{-1} h^{-1} at temperatures between 300 and 400 °C and pressures up to 5.5 MPa. To enable a more meaningful comparison across different studies, activities here are primarily discussed on NH_3 synthesis rates normalized to Ru mass (in mmol NH_3 g_{Ru}^{-1} h^{-1}). According to these values, our Ba-Ru/CN-A catalyst shows better performance than state-of-the-art Ru-based systems. This enhanced activity per unit mass of Ru suggests more efficient utilisation of the noble metal, likely due to the formation of highly active Ru–BaO interfaces that facilitate N_2 activation. Similar interfacial effects have been reported previously. For instance, Ogura et al. [30,31] found that the interface between metal and metal oxides, in their case Ru and LaCe, can facilitate the activation of nitrogen bond, enabling NH_3 synthesis under unexpectedly mild conditions. In related studies, Baik et al. [28,43] have further shown that BaO is among the most effective promoters for Ru-based catalysts, outperforming alkali promoters (such as CsO) under comparable conditions. The authors of the corresponding publications obtained very similar results to those in this manuscript, but at significantly higher weight hourly space velocities (WHSV). Remarkably, our Ba-Ru/CN-A catalyst achieved significant ammonia synthesis activity at thermocouple-measured catalyst bed temperatures as low as 350 °C, which is below the typical operating temperatures reported for similar catalysts. This low temperature activity is particularly favourable for integration with renewable energy sources, where lower operating temperatures can lead to improved energy efficiency.

Unlike external thermal heating, magnetic heating delivers energy directly to the magnetically active component of the catalyst, resulting in localized heating of the active sites. This method of energy delivery minimizes heat losses associated with reactor walls and heat-transfer media, and substantially reduces the system's thermal inertia. Consequently, the local temperature at the catalytically active sites can exceed the apparent bulk temperature measured in the catalyst bed, consistent with the temperature offsets inferred from kinetic analysis and calorimetric measurements. This localized overheating provides a mechanistic explanation for the rapid attainment of steady-state operation and the pronounced dynamic response observed during magnetic field switching.

However, it should be acknowledged that under the investigated conditions the ammonia yields at the T_bed of maximum activity remain well below the corresponding thermodynamic equilibrium values. This behavior reflects a fundamental kinetic–thermodynamic trade-off inherent to all exothermic equilibrium limited processes, but

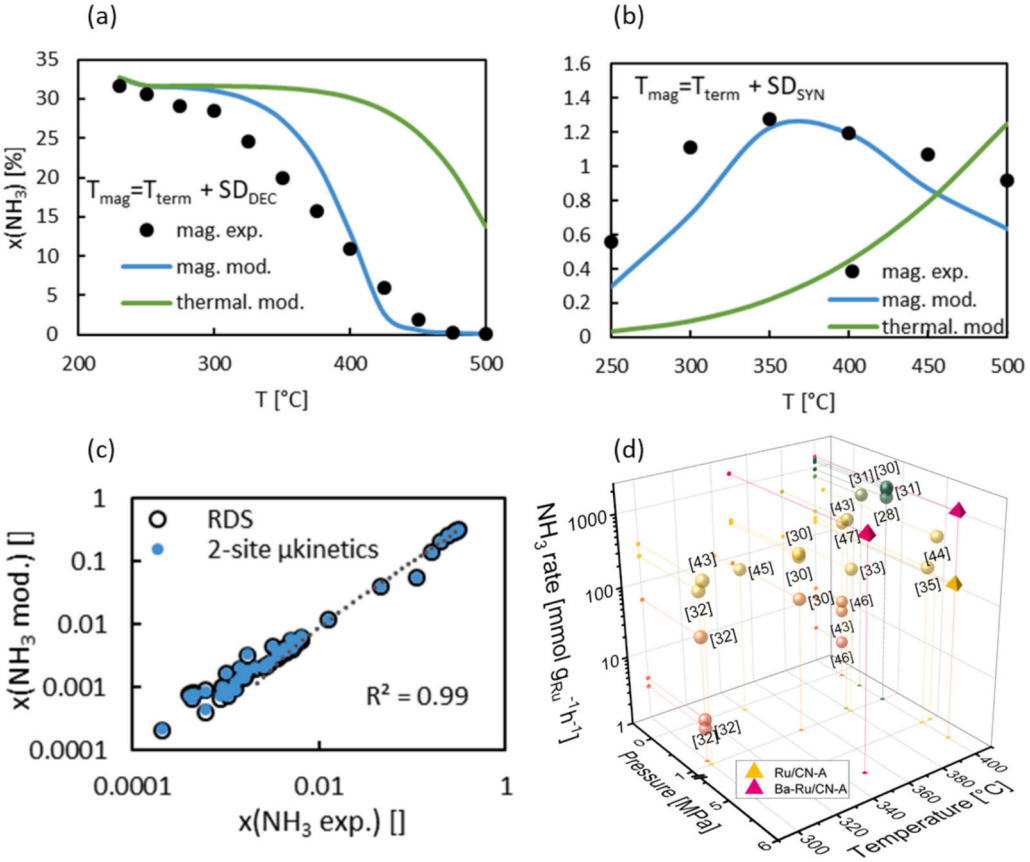

Fig. 10. Modelling of (a) NH_3 decomposition and (b) NH_3 synthesis with(out) temperature correction to consider magnetic heating. (c) Parity plot of microkinetic and lumped (RDS assumption). (d) Comparison of the performance of our catalysts with Ru-based catalysts reported in the literature. Values marked with [X] correspond to the respective references.

Table 2
Comparison of ammonia performance of Ru-based catalysts.

Ref.	Catalyst	T [°C]	p [MPa]	NH_3 rate [mmol g_{cat}^{-1} h^{-1}]	NH_3 rate [mmol g_{Ru}^{-1} h^{-1}]
Our results	Ba-Ru/CN-A	350[a]	5.5	12.56	1551
Our results	Ba-Ru/CN-A	400[a]	5.5	11.58	1430
Our results	Ru/CN-A	400[a]	5.5	1.28	158
[44]	Ru-Ba/MgO100	405	5	22.10	442
[28]	0.75Ba-Ru/MgO	400	1	47.25	945
[33]	0.5Ba-10Ru/MPC	380	0.99	10.40	128
[35]	Ru-Ba-Al_2O_3	400	5	9.07	181
[45]	Ru/Ba–Ca(NH2)2	340	0.1	12.40	124
[46]	Ba-Ru/AC	400	0.1	0.15	15
[32]	Ru/Ba-Ca$(NH_2)_2$	300	0.9	23.3	233
[32]	Ru/Ba-$(NH_2)_2$	300	0.9	0.3	3
[43]	Ba-Ru/N-MWNT-1	300	1	17.12	342
[46]	Ru/γ-Al_2O_3	400	0.1	0.05	3
[46]	Cs-Ru@MgO	400	0.1	2.26	226
[46]	Ru/CaO	400	0.1	0.16	11
[30]	Ru/CeO_2	350	1	17.20	344
[30]	Ru/Pr_2O_3	350	1	15.70	314
[30]	Ru/$La_{0.5}Ce_{0.5}O_{1.75}$	400	1	65	1300
[30]	Cs^+/Ru/MgO	350	1	4.1	82
[47]	Cs-Ru/SGCNT	380	0.9	58.2	582
[32]	Cs-Ru/MgO	300	0.9	0.40	4
[32]	Ru/Ca$(NH_2)_2$	300	0.9	5.7	57
[31]	Ru/$La_{0.5}Pr_{0.5}O_{1.75}$	400	1	60.2	1204
[31]	Ru/$La_{0.5}Pr_{0.5}O_{1.75}$	400	0.5	37.1	742

[a] Temperatures refer to thermocouple-measured catalyst bed temperatures (T_bed).

exaggerated in magnetically heated operation. While localized high temperatures promote fast reaction kinetics and excellent dynamic responsiveness, they simultaneously limit equilibrium-controlled single-pass conversion. This barrier, however, is not critical, as the exothermic nature of the NH₃ synthesis reaction can provide sufficient energy to offset heat losses once a certain reactor scale or degree of thermal insulation is reached, thereby minimizing the need for additional heating under steady-state operation. From a process design perspective, this may impose constraints on downstream separation and overall process efficiency. Recent process-oriented study [48] has highlighted that such limitations can be mitigated through established strategies, including recycle or multi-pass operation, and staged reactor concepts with spatial or temporal temperature zoning. Operation at higher pressures is generally constrained by the pressure limitations of quartz reactor tubes. In this context, the present results highlight that the primary advantage of magnetic heating is not a fundamentally altered catalytic mechanism, but rather its ability to enable rapid, localized, and dynamically controllable heating that is difficult to achieve using external thermal heating. While single-pass ammonia yields remain below equilibrium, this operating regime may be particularly advantageous for electrified, modular process concepts, where rapid start-up, flexible load-following operation, and integration with intermittent renewable energy sources are prioritized over equilibrium-limited performance.

Finally, it is important to emphasize that this study focuses on a deliberately integrated catalyst–heating concept, where a magnetically active support is required to enable magnetic heating. Therefore, the results should not be interpreted as a universal comparison between magnetic and conventional heating for arbitrary catalyst systems, but rather as a proof-of-concept demonstration of magnetically heated ammonia synthesis under elevated pressure conditions.

5. Conclusion

In summary, we have developed a magnetically active, Ba-promoted Ru/CN-A composite catalyst that enables electrified and adaptable ammonia synthesis. For this purpose, a custom-designed, magnetically heated reactor operating at pressures up to 5.5 MPa was developed. The favourable effect of Ba, which increases the reaction rate by a factor of ten (>1500 mmol NH_3 g_{Ru}^{-1} h^{-1}), was attributed to the reduced nitrogen dissociation energy at the Ba—Ru interfaces. An important finding of this study is that magnetic heating leads to substantially elevated effective temperatures at the catalytically active sites. Microkinetic modelling and calorimetric measurements consistently show that these temperatures exceed the thermocouple-measured catalyst bed temperature by more than 100 °C, providing a mechanistic explanation for the observed high reaction rates and rapid thermal response. As a result, steady-state ammonia synthesis is achieved in within approximately 10 min, a time scale short enough to operate the reactor efficiently with intermittent renewable electricity.

CRediT authorship contribution statement

A. Sedminek: Writing – review & editing, Writing – original draft, Methodology, Investigation, Formal analysis, Conceptualization. **D. Makovec:** Writing – review & editing, Writing – original draft, Investigation. **M. Huš:** Writing – original draft, Investigation. **A. Prašnikar:** Writing – original draft, Investigation. **S. Yakushkin:** Writing – original draft, Investigation. **B. Likozar:** Funding acquisition. **J. Teržan:** Writing – review & editing, Writing – original draft, Supervision, Methodology, Investigation, Conceptualization. **S. Gyergyek:** Writing – review & editing, Supervision, Funding acquisition, Conceptualization.

Declaration of competing interest

A.S., J.T., B.L, D.M. and. S.G. are listed as co-inventors on the patent WO/2025/162843, titled “Fast Dynamically Responsive Ammonia Synthesis or Cracking for H_2 Storage Utilising Structured Magnetically-heated Catalysts”. The patent describes a method for quickly tuneable on-demand gas phase reactions of ammonia decomposition to produce hydrogen and nitrogen gas and the reversible reaction of ammonia synthesis from hydrogen and nitrogen gas by the use of magnetic heating, the corresponding catalyst materials, their preparation procedures and a reactor system designed specifically for gas-phase magnetic catalysis. The remaining authors declare no competing interests.

Acknowledgements

A.S., J.T. and S.G. acknowledge support from the European Union's

Horizon 2020 Research and Innovation Program under Grant agreement no. 101022738 and the European Union NextGenerationEU through project HyBReED. J.T., S. Y., A.P. and B.L. appreciate the funding from the Slovenian Research Agency (ARIS) through program P2-0152, A.P. acknowledge support from the European Union's Horizon 2020 Research and Innovation program under Grant agreement no. 101058643, D.M. and S.G. were funded through core program P2-0089. M.H. appreciates infrastructure funding I0-0039 and project funding J2-70085 from ARIS. Anej Blažič and Žiga Ponikvar are kindly acknowledged for their assistance in catalyst synthesis. Petra Jenuš is kindly acknowledged for VSM measurements.

Appendix A. Supplementary data

Supplementary data to this article can be found online at https://doi.org/10.1016/j.cej.2026.175068.

Data availability

Data will be made available on request.

References

[1] Z. Abdin, A. Zafaranloo, A. Rafiee, W. Mérida, W. Lipiński, K.R. Khalilpour, Hydrogen as an energy vector, Renew. Sust. Energ. Rev. 120 (2020) 109620, https://doi.org/10.1016/j.rser.2019.109620.
[2] S. Chatterjee, R.K. Parsapur, K.-W. Huang, Limitations of ammonia as a hydrogen energy carrier for the transportation sector, ACS Energy Lett. 6 (12) (2021) 4390–4394, https://doi.org/10.1021/acsenergylett.1c02189.
[3] M. Aziz, A.T. Wijayanta, A.B.D. Nandiyanto, Ammonia as effective hydrogen storage: a review on production, storage and utilization, Energies 13 (12) (2020) 3062, https://doi.org/10.3390/en13123062.
[4] Z. Zhao, M. Zhang, Y. Wu, W. Song, J. Yan, X. Qi, J. Yang, J. Wen, H. Zhang, Ammonia energy: synthesis and utilization, Ind. Eng. Chem. Res. 63 (18) (2024) 8003–8024, https://doi.org/10.1021/acs.iecr.4c00384.
[5] F. Tian, N. Zhou, W. Chen, J. Zhan, L. Tang, M. Wu, Progress in green ammonia synthesis technology: catalytic behavior of ammonia synthesis catalysts, Adv. Sustainable Syst. (2024) 2300618, https://doi.org/10.1002/adsu.202300618.
[6] V. Shahed Gharahshiran, Y. Zheng, Sustainable Ammonia synthesis: an in-depth review of non-thermal plasma technologies, J. Energy Chem. 96 (2024) 1–38, https://doi.org/10.1016/j.jechem.2024.04.018.
[7] A.J. Martín, T. Shinagawa, J. Pérez-Ramírez, Electrocatalytic reduction of nitrogen: from Haber-Bosch to ammonia artificial leaf, Chem 5 (2) (2019) 263–283, https://doi.org/10.1016/j.chempr.2018.10.010.
[8] Y. Zhang, J. Niu, S. Chen, Y. Chen, H. Chen, X. Fan, Ammonia synthesis by nonthermal plasma catalysis: a review on recent research progress, J. Phys. D. Appl. Phys. 57 (32) (2024) 323001, https://doi.org/10.1088/1361-6463/ad4717.
[9] W. Wang, G. Tuci, C. Duong-Viet, Y. Liu, A. Rossin, L. Luconi, J.-M. Nhut, L. Nguyen-Dinh, C. Pham-Huu, G. Giambastiani, Induction heating: an enabling technology for the heat management in catalytic processes, ACS Catal. 9 (9) (2019) 7921–7935, https://doi.org/10.1021/acscatal.9b02471.
[10] J. Mazarío, S. Ghosh, V. Varela-Izquierdo, L.M. Martínez-Prieto, B. Chaudret, Magnetic nanoparticles and radio frequency induction: from specific heating to magnetically induced catalysis, ChemCatChem (2024) e202400683, https://doi.org/10.1002/cctc.202400683.
[11] S. Gyergyek, A. Kocjan, M. Grilc, B. Likozar, B. Hočevar, D. Makovec, A hierarchical Ru-bearing alumina/magnetic iron-oxide composite for the magnetically heated hydrogenation of furfural, Green Chem. 22 (18) (2020) 5978–5983, https://doi.org/10.1039/D0GC00966K.
[12] J.-S. Pavelić, S. Gyergyek, B. Likozar, M. Grilc, Process electrification by magnetic heating of catalyst, Chem. Eng. J. 505 (2025) 158928, https://doi.org/10.1016/j.cej.2024.158928.
[13] H. Liu, W. Han, Wüstite-based catalyst for ammonia synthesis: structure, property and performance, Catal. Today 297 (2017) 276–291, https://doi.org/10.1016/j.cattod.2017.04.062.
[14] S.O.S. Batista, M.A. Morales, W.C. dos Santos, C.A. Iglesias, E. Baggio-Saitovitch, A. S. Carriço, F. Bohn, S.N. de Medeiros, Mechano-synthesis, structural and magnetic characterization, and heat release of α-Fe nanoparticles embedded in a Wüstite matrix, J. Magn. Magn. Mater. 391 (2015) 83–88, https://doi.org/10.1016/j.jmmm.2015.04.112.
[15] M. Gheisari, M. Mozaffari, M. Acet, J. Amighian, Preparation and investigation of magnetic properties of Wüstite nanoparticles, J. Magn. Magn. Mater. 320 (21) (2008) 2618–2621, https://doi.org/10.1016/j.jmmm.2008.05.028.
[16] M.R. Almind, M.G. Vinum, S.T. Wismann, M.F. Hansen, S.B. Vendelbo, J. S. Engbæk, P.M. Mortensen, I. Chorkendorff, C. Frandsen, Optimized CoNi nanoparticle composition for curie-temperature-controlled induction-heated catalysis, ACS Appl. Nano Mater. 4 (11) (2021) 11537–11544, https://doi.org/10.1021/acsanm.1c01941.
[17] A. Sedminek, D. Makovec, J. Teržan, B. Likozar, P. Jenuš, A. Kocjan, G. Marolt, S. Gyergyek, Scalable method for the preparation of CoxNi1-x/alumina nanocomposites and their magnetic heating properties, J. Alloys Compd. 1005 (2024) 176109, https://doi.org/10.1016/j.jallcom.2024.176109.
[18] G. Saso, K. Andraz, M. Darko, Method for Synthesis of Coated Magnetic Particles. GB2582272B, 2021.
[19] G. Kresse, J. Hafner, Ab initio molecular dynamics for liquid metals, Phys. Rev. B 47 (1) (1993) 558–561, https://doi.org/10.1103/PhysRevB.47.558.
[20] G. Kresse, J. Furthmüller, Efficiency of ab-initio total energy calculations for metals and semiconductors using a plane-wave basis set, Comput. Mater. Sci. 6 (1) (1996) 15–50, https://doi.org/10.1016/0927-0256(96)00008-0.
[21] G. Kresse, J. Furthmüller, Efficient iterative schemes for ab initio total-energy calculations using a plane-wave basis set, Phys. Rev. B 54 (16) (1996) 11169–11186, https://doi.org/10.1103/PhysRevB.54.11169.
[22] J.P. Perdew, K. Burke, M. Ernzerhof, Generalized gradient approximation made simple, Phys. Rev. Lett. 77 (18) (1996) 3865–3868, https://doi.org/10.1103/PhysRevLett.77.3865.
[23] J.P. Perdew, K. Burke, M. Ernzerhof, Generalized gradient approximation made simple [Phys. Rev. Lett. 77, 3865 (1996)], Phys. Rev. Lett. 78 (7) (1997) 1396, https://doi.org/10.1103/PhysRevLett.78.1396.
[24] S. Grimme, J. Antony, S. Ehrlich, H. Krieg, A consistent and accurate ab initio parametrization of density functional dispersion correction (DFT-D) for the 94 elements H-Pu, J. Chem. Phys. 132 (15) (2010) 154104, https://doi.org/10.1063/1.3382344.
[25] G. Makov, M.C. Payne, Periodic boundary conditions in ab initio calculations, Phys. Rev. B 51 (7) (1995) 4014–4022, https://doi.org/10.1103/PhysRevB.51.4014.
[26] A. Heyden, A.T. Bell, F.J. Keil, Efficient methods for finding transition states in chemical reactions: comparison of improved dimer method and partitioned rational function optimization method, J. Chem. Phys. 123 (22) (2005) 224101, https://doi.org/10.1063/1.2104507.
[27] G. Henkelman, H. Jónsson, A dimer method for finding saddle points on high dimensional potential surfaces using only first derivatives, J. Chem. Phys. 111 (15) (1999) 7010–7022, https://doi.org/10.1063/1.480097.
[28] Y. Baik, M. Kwen, K. Lee, S. Chi, S. Lee, K. Cho, H. Kim, M. Choi, Splitting of hydrogen atoms into proton–electron pairs at BaO–Ru interfaces for promoting ammonia synthesis under mild conditions, J. Am. Chem. Soc. 145 (20) (2023) 11364–11374, https://doi.org/10.1021/jacs.3c02529.
[29] O. Karslıoğlu, L. Trotochaud, I. Zegkinoglou, H. Bluhm, X-ray spectroscopic characterization of BaO, Ba(OH)2, BaCO3, and Ba(NO3)2, J. Electron Spectrosc. Relat. Phenom. 225 (2018) 55–61, https://doi.org/10.1016/j.elspec.2018.03.008.
[30] Y. Ogura, K. Sato, S. Miyahara, Y. Kawano, T. Toriyama, T. Yamamoto, S. Matsumura, S. Hosokawa, K. Nagaoka, Efficient ammonia synthesis over a Ru/La0.5Ce0.5O1.75 catalyst pre-reduced at high temperature, Chem. Sci. 9 (8) (2018) 2230–2237, https://doi.org/10.1039/C7SC05343F.
[31] Y. Ogura, K. Tsujimaru, K. Sato, S. Miyahara, T. Toriyama, T. Yamamoto, S. Matsumura, K. Nagaoka, Ru/La0.5Pr0.5O1.75 catalyst for low-temperature ammonia synthesis, ACS Sustain. Chem. Eng. 6 (12) (2018) 17258–17266, https://doi.org/10.1021/acssuschemeng.8b04683.
[32] M. Kitano, Y. Inoue, M. Sasase, K. Kishida, Y. Kobayashi, K. Nishiyama, T. Tada, S. Kawamura, T. Yokoyama, M. Hara, H. Hosono, Self-organized ruthenium–barium core–shell nanoparticles on a mesoporous calcium amide matrix for efficient low-temperature ammonia synthesis, Angew. Chem. Int. Ed. 57 (10) (2018) 2648–2652, https://doi.org/10.1002/anie.201712398.
[33] M. Nishi, S.-Y. Chen, H. Takagi, Mild Ammonia synthesis over Ba-promoted Ru/MPC catalysts: effects of the Ba/Ru ratio and the mesoporous structure, Catalysts 9 (5) (2019) 480, https://doi.org/10.3390/catal9050480.
[34] E. Truszkiewicz, W. Raróg-Pilecka, K. Schmidt-Szałowski, S. Jodzis, E. Wilczkowska, D. Łomot, Z. Kaszkur, Z. Karpiński, Z. Kowalczyk, Barium-promoted Ru/carbon catalyst for ammonia synthesis: state of the system when operating, J. Catal. 265 (2) (2009) 181–190, https://doi.org/10.1016/j.jcat.2009.04.024.
[35] B. Lin, L. Heng, B. Fang, H. Yin, J. Ni, X. Wang, J. Lin, L. Jiang, Ammonia synthesis activity of alumina-supported ruthenium catalyst enhanced by alumina phase transformation, ACS Catal. 9 (3) (2019) 1635–1644, https://doi.org/10.1021/acscatal.8b03554.
[36] C.J. Bardwell, R.I. Bickley, S. Poulston, M.V. Twigg, Thermal decomposition of bulk and supported barium nitrate, Thermochim. Acta 613 (2015) 94–99, https://doi.org/10.1016/j.tca.2015.05.013.
[37] S.R. Kulkarni, N. Realpe, A. Yerrayya, V.K. Velisoju, S. Sayas, N. Morlanes, J. Cerillo, S.P. Katikaneni, S.N. Paglieri, B. Solami, J. Gascon, P. Castaño, Elucidating the rate-determining step of ammonia decomposition on Ru-based catalysts using ab initio-grounded microkinetic modeling, Cat. Sci. Technol. 13 (7) (2023) 2026–2037, https://doi.org/10.1039/D3CY00055A.
[38] P. Feulner, D. Menzel, The adsorption of hydrogen on ruthenium (001): adsorption states, dipole moments and kinetics of adsorption and desorption, Surf. Sci. 154 (2) (1985) 465–488, https://doi.org/10.1016/0039-6028(85)90045-7.
[39] S. Dahl, E. Törnqvist, I. Chorkendorff, Dissociative adsorption of N2 on Ru(0001): a surface reaction totally dominated by steps, J. Catal. 192 (2) (2000) 381–390, https://doi.org/10.1006/jcat.2000.2858.
[40] Z. Zhang, C. Karakaya, R.J. Kee, J.D. Way, C.A. Wolden, Barium-promoted ruthenium catalysts on yittria-stabilized zirconia supports for ammonia synthesis, ACS Sustain. Chem. Eng. 7 (21) (2019) 18038–18047, https://doi.org/10.1021/acssuschemeng.9b04929.

[41] J. Zhang, H. Xu, Q. Ge, W. Li, Highly efficient Ru/MgO catalysts for NH3 decomposition: synthesis, characterization and promoter effect, Catal. Commun. 7 (3) (2006) 148–152, https://doi.org/10.1016/j.catcom.2005.10.002.
[42] W. Zheng, J. Zhang, H. Xu, W. Li, NH3 decomposition kinetics on supported Ru clusters: morphology and particle size effect, Catal. Lett. 119 (3) (2007) 311–318, https://doi.org/10.1007/s10562-007-9237-z.
[43] Y. Baik, S. Chi, K. Lee, D. Oh, K. Lee, M. Choi, Electron and proton storage on separate Ru and BaO domains mediated by conductive low-work-function carbon to accelerate ammonia synthesis, Nat. Catal. 8 (3) (2025) 248–256, https://doi.org/10.1038/s41929-025-01302-z.
[44] K. Lee, R. Woo, H.C. Woo, G. Ko, K. Cho, Y. Park, M. Choi, H.C. Yoon, Unraveling the role of MgO in the Ru-Ba/MgO catalyst for boosting ammonia synthesis: comparative study of MgO and MgAlO*x* supports, J. Catal. 434 (2024) 115530, https://doi.org/10.1016/j.jcat.2024.115530.
[45] M. Hattori, T. Mori, T. Arai, Y. Inoue, M. Sasase, T. Tada, M. Kitano, T. Yokoyama, M. Hara, H. Hosono, Enhanced catalytic ammonia synthesis with transformed BaO, ACS Catal. 8 (12) (2018) 10977–10984, https://doi.org/10.1021/acscatal.8b02839.
[46] M. Kitano, Y. Inoue, Y. Yamazaki, F. Hayashi, S. Kanbara, S. Matsuishi, T. Yokoyama, S.-W. Kim, M. Hara, H. Hosono, Ammonia synthesis using a stable electride as an electron donor and reversible hydrogen store, Nat. Chem. 4 (11) (2012) 934–940, https://doi.org/10.1038/nchem.1476.
[47] M. Nishi, S.-Y. Chen, H. Tateno, T. Mochizuki, H. Takagi, T. Nanba, A super-growth carbon nanotubes-supported, Cs-promoted Ru catalyst for 0.1–8 MPaG ammonia synthesis, J. Catal. 413 (2022) 623–635, https://doi.org/10.1016/j.jcat.2022.07.015.
[48] K. Lee, H.C. Yoon, S.H. Kim, J. Shim, J.H. Kim, T.-S. Kim, Key engineering criteria for developing next-generation catalysts in advanced Haber–Bosch ammonia synthesis process: from laboratory studies to commercialization, Mol. Catal. 572 (2025) 114781, https://doi.org/10.1016/j.mcat.2024.114781.